THE ASTROPHYSICAL JOURNAL, 406:457–469, 1993 April 1

SPIRAL STRUCTURE OF THE GIANT GALAXY UGC 2885: Hα KINEMATICS

BLAISE CANZIAN[1] AND R. J. ALLEN[1,2]
Space Telescope Science Institute, 3700 San Martin Drive, Baltimore, MD 21218
AND
R. P. J. TILANUS[2]
Owens Valley Radio Observatory, P.O. Box 968, Big Pine, CA 93513
Received 1991 July 29; accepted 1992 September 30

ABSTRACT

The velocity field of the exceptionally large Sc galaxy UGC 2885 (Holmberg radius 84 h^{-1} kpc, where $h = H_0/100$ km s^{-1} Mpc^{-1}) has been mapped in Hα emission with the TAURUS I imaging Fabry-Perot spectrometer using the 2.5 m telescope at La Palma. The rotation curve extracted from the velocity field agrees with published data. Ripples in the velocity field around the minor axis indicate radial flows across the spiral arms. The radial flow speeds in the plane of the disk show 50–70 km s^{-1} peak-to-peak variation, suggesting that a strong density wave is present in the underlying stellar disk. Such high speeds may alternatively be a natural consequence of the open arm spiral pattern. In addition, strong density waves may naturally occur in large spiral galaxies or in spiral galaxies as massive as UGC 2885. (Its mass is over 10^{12} h^{-1} $M_\odot$ within the radius to which spiral arms reach, 52 h^{-1} kpc.) A strong density wave may also be necessary for the effective maintenance of the orderly, two-armed spiral pattern that is visible in the outer disk of UGC 2885, where the gas has made only about a dozen revolutions in a Hubble time.

Subject headings: galaxies: individual (UGC 2885) — galaxies: kinematics and dynamics — galaxies: spiral — techniques: interferometric

1. INTRODUCTION

1.1. *Background and Motivation*

How well does observed spiral arm morphology and velocity structure compare with predictions of spiral density wave theory? The nonlinear response of gas to a spiral perturbation in the gravitational potential was detailed by Shu, Milione, & Roberts (1973). They calculated the variation of the velocity of the gas owing to spiral density waves in a stellar disk for several galaxy models. In their results, radial flow speeds in the disk do not exceed 20 km s^{-1} for modest spiral potentials (≈5% perturbations on the axisymmetric potential). Inside the corotation radius, gas interior to an arm is accelerated outward toward the arm, and gas just exterior to the arm moves inward. The few high-resolution observations that have been made to date do not all corroborate theory to the same extent, and sometimes there are conflicting results for the same galaxy. Visser (1980a, b) found good agreement between the computed gas response to an imposed linear density wave (Roberts 1969) and the observed H I density and velocity in M81 within the limited resolution of the available observations (25″ ≈ 400 pc). Radial motions of the H I perpendicular to spiral arms were about 10 km s^{-1} in magnitude. In contrast, the radial motions of the molecular gas in M51 measured with CO observations (Vogel, Kulkarni, & Scoville 1988) are larger, 60–90 km s^{-1}, but properly directed according to theory. Tilanus & Allen (1991) detected no radial motion across the arms of M51 in the H I exceeding 30 km s^{-1}, although streaming motions similar to those in the CO were found in Hα. Two spiral galaxies with well-defined arms have failed to show streaming motions in independent Fabry-Perot emission line studies: M83 (Tilanus 1990; Tilanus & Allen 1992) and NGC 1566 (Pence, Taylor, & Atherton 1990). While the slight and uncertain inclination of M83 makes detection of spiral density wave streaming motions difficult, the case of NGC 1566 is problematic because it is quite inclined ($i = 41°$).

The confusing results of velocity studies using various tracers of spiral structure suggest that different tracers inform us about different parts of the velocity field. Spatial displacement of the H I arms in M51 from the nonthermal continuum arms (which are, in turn, coincident with dust lanes: Tilanus & Allen 1989) and separation of H I from the dust lanes in M83 (Allen, Atherton, & Tilanus 1986) suggest that H I is a dissociation product of H_2 in spiral arm molecular clouds (Allen et al. 1986; Tilanus & Allen 1991). The composition of the interstellar medium evidently changes across spiral arms in these galaxies. Different spiral arm tracers would then indicate motions at different phases of a passing spiral density wave, so agreement among studies using different tracers is not necessarily expected. A comparison between theory and observation therefore becomes a complicated mixture of density wave-driven streaming motions, the physics of star formation, and the effects of shocks and H II regions on the surrounding interstellar medium.

1.2. *The Galaxy UGC 2885*

UGC 2885 is an enormous spiral galaxy, a fact pointed out by Rubin, Ford, & Thonnard (1980). A distance to the galaxy of 56.8 h^{-1} Mpc (where $h = H_0/100$ km s^{-1} Mpc^{-1}) is estimated from its systemic velocity of 5794 km s^{-1} (Roelfsema & Allen 1985) by converting this heliocentric velocity to motion relative to the Local Group (Sandage & Tammann 1981) and then referring this motion to the cosmic microwave background (Smoot et al. 1991). (See Table 1 for the Galactic coordinates of UGC 2885.) The result is a Hubble velocity of

[1] The Space Telescope Science Institute is operated by the Association of Universities for Research in Astronomy, Inc. under contract with the National Aeronautics and Space Administration.
[2] Also Kapteyn Astronomical Institute, Groningen, The Netherlands.

(5683 ± 22) km s^{-1}, which implies a scale of 276 h^{-1} pc arcsec^{-1} along the major axis of the galaxy. The spiral structure in the inner disk of UGC 2885 (inside 10 h^{-1} kpc radius) is complex, but the outer disk displays a well-defined, two-armed spiral pattern. The rotation curve, measured by Rubin et al. (1980; but see Burstein et al. 1982) and extended by Roelfsema & Allen (1985), rises steeply and then remains flat to an extraordinarily large distance from the center: the farthest H I datum is at 190″ radius, or 52 h^{-1} kpc. The circular speed there, 298 km s^{-1}, implies a mass of at least 1.1 $h^{-1} \times 10^{12}$ $M_\odot$ within that radius. The gas in the spiral arms of UGC 2885 at the farthest measured point on the optical rotation curve (at 39 h^{-1} kpc radius) has made only a dozen revolutions in a Hubble time, independent of H_0. Because UGC 2885 lies at low Galactic latitude ($b = -14°$) near the California Nebula (NGC 1499), accurate estimation of Galactic extinction is difficult; the optical diameter of UGC 2885 based on the UGC "a" diameter (Nilson 1973) is $D_{25} = 91\ h^{-1}$ kpc and the Holmberg radius is estimated to be $R_{Ho} = 5'.1 = 84\ h^{-1}$ kpc (Rubin et al. 1980). The scale length of the exponential disk of UGC 2885 is about 8.6 h^{-1} kpc, based on near-infrared photometry by Giovanardi & Hunt (1988).

For comparison, H I data (Guhathakurta et al. 1988) for the bright spiral NGC 4321 in the Virgo Cluster extends to 18 kpc (assuming a distance of 14.7 Mpc: Jacoby, Ciardullo, & Ford 1990), enclosing a mass of at least 1.9×10^{11} $M_\odot$, making this galaxy 3 times smaller and one-tenth as massive as UGC 2885. H I data for M31 (Roberts & Whitehurst 1975) extend to 30 kpc (assuming a distance of 690 kpc) and enclose a mass of at least 3.8×10^{11} $M_\odot$, making it at most half the size and a quarter the mass of UGC 2885. The Holmberg radius of M101, a giant Sc galaxy, is 14'.0 (Huchtmeier 1975), or only 29 kpc if its distance is 7.2 Mpc, making it only one-third the size of UGC 2885. The radius of the last-measured H I datum for M101 is 45', where the rotation speed is 175 km s^{-1} (Huchtmeier 1975), implying a total mass for M101 of 6.7×10^{11} $M_\odot$, making it half as massive as UGC 2885.

The above comparisons illustrate the exceptional size of UGC 2885. Partly because of this large size and partly because of the regular, two-armed spiral pattern that spans a large range of radii in the outer parts of the galaxy, Roelfsema & Allen (1985) suggested that the corotation resonance of the pattern may occur at a radius that is well within the visible disk. In that case, a kinematic signature of corotation may be found in the streaming motions of the gas. However, the resolution of the H I observations available to Roelfsema & Allen (13 × 23 arcsec^2) was not sufficient to separate spiral arms. The present observations were therefore carried out to achieve a detailed mapping of the streaming velocities that resolves the spiral arms.

1.3. *The Main Result*

The imaging Fabry-Perot spectrometer data in the Hα emission line presented in this paper indicate large radial flow velocities across spiral arms in the galaxy UGC 2885. The radial velocities in the plane of the disk, spanning 50–70 km s^{-1} peak-to-peak on each side of the galaxy, are so large that they may signify an exceptionally strong spiral density wave. However, large radial flow velocities are expected if the pattern is open (§ 4), so the radial flow velocities reported here may be normal. A comparison with spiral density wave theory will be presented in a later paper; here, we will concentrate on a discussion of the observations we have made and on our main observational results.

2. OBSERVATIONS

Hα emission from UGC 2885 was observed 1985 October 21–22 with the TAURUS-I imaging Fabry-Perot spectrometer (Atherton et al. 1982) on the 2.5 m Isaac Newton telescope at La Palma. The spacing of the etalon (gap about 112 μm) was repeatedly stepped up and down through the free spectral range (19.9 Å, or 910 km s^{-1} at 6691 Å, corresponding to the wavelength of Hα redshifted to the heliocentric systemic velocity of the galaxy) in a quick-scanning mode in which the integration time was only 10 s per step. This procedure was motivated by a desire to counteract the effects of changing seeing during the scanning. Frames were recorded in digital form at each step using an IPCS detector (Boksenberg 1972) and co-added at corresponding etalon spacings. A total of nearly 10.5 hr of integration on UGC 2885 in 25 cycles of gap spacing was accumulated during the two nights. There was some contamination by sunlight reflected from the Moon, whose disk was illuminated 50%–55% during the observations. Sunlight reflected from the Moon could have perturbed our velocity profiles, but our data processing procedure (described later) removes its effect. The Hα line was observed in order 335 using a prefilter nominally centered at 6689 Å with nominal width of 15 Å (FWHM). The wavelength of Hα redshifted to the systemic velocity of UGC 2885 (see Table 1) is 6690.86 Å, nearly 2 Å different from the prefilter's nominal center. The asymptotic rotation speed of UGC 2885 is $V_\infty =$ 298 km s^{-1} (Roelfsema & Allen 1985). We therefore expect the total width of Hα emission to be $2V_\infty \sin i = 524$ km s^{-1} or 11.5 Å at the wavelength of redshifted Hα, where $i = 62°$ is the inclination (Table 1).

The narrowness of the prefilter implies that little error in central wavelength can be tolerated. We chose to establish independently the actual placement of the prefilter by examining the spectrum of a bright star in the field. Figure 1 shows this spectrum. The response of the Fabry-Perot spectrometer at each spacing consists of a comb of sharp peaks separated by the free spectral range (Fabry & Perot 1902; also, e.g., Vaughan 1989, p. 100) multiplied by the prefilter function. Therefore, Figure 1 contains contributions not only from the etalon response peak near the prefilter center but also from the peaks adjacent to it. Assuming that the actual spectrum of the star is flat over the range in wavelength observed and that the

TABLE 1

UGC 2885 PHYSICAL PARAMETERS

Parameter	Value
α_{1950}[a]	03^{h}49^{m}48^s.5
δ_{1950}[a]	+35°26′30″.0
l	159°.7
b	−14°.2
V_{sys}[b] (km s^{-1})	5794 ± 10
Distance (Mpc)	56.8 h^{-1}
Scale (pc arcsec^{-1})	276 h^{-1}
Position Angle	225° ± 2°
Inclination	62° ± 2°
V_{circ}[c] (∞) (km s^{-1})	298
R_{Ho}[d] (kpc)	84 h^{-1}

[a] ±4″.
[b] Heliocentric.
[c] Roelfsema & Allen 1985.
[d] Rubin et al. 1980.

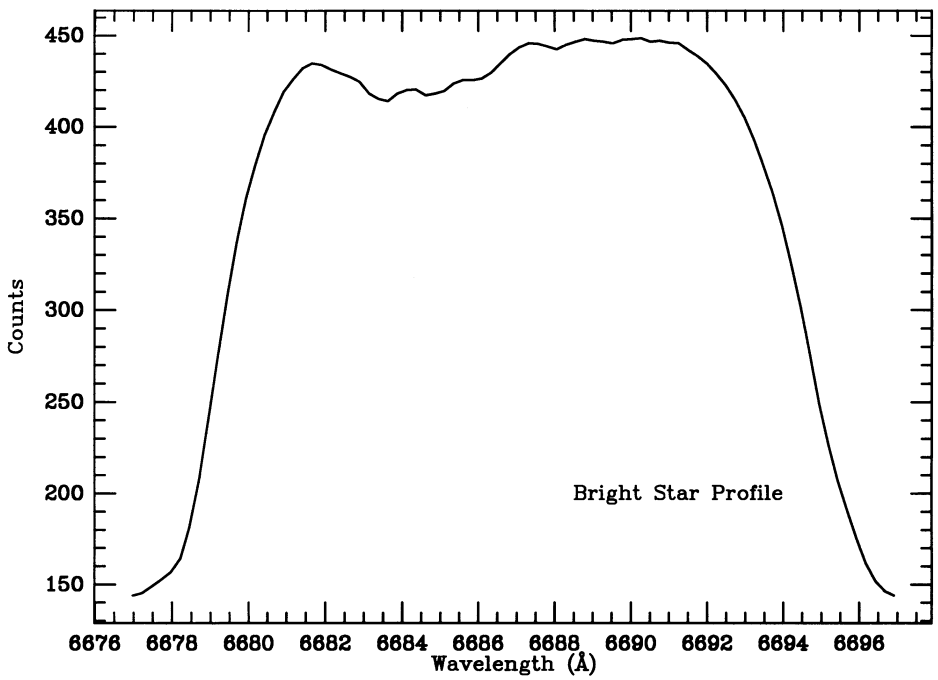

FIG. 1.—Spectrum of a bright star in the field measured by the Fabry-Perot spectrometer. Each wavelength includes aliased contributions, attenuated by the prefilter, from an integral number of free spectral ranges away.

response of the etalon is an array of delta functions separated by the free spectral range, we have estimated the shape of the prefilter using an iterative procedure. The reconstructed prefilter shape is shown in Figure 2; the central part of the filter response is well determined, but the wings are less constrained. From Figure 2, we see that the prefilter has a width of about 16 Å (FWHM) and is actually centered at about 6687 Å, which is about 4 Å below the redshifted Hα in the galaxy.

The integrated Hα spectrum of UGC 2885 constructed from our data is also shown in Figure 2 with an arbitrary scale. Hα emission from the more redshifted side of UGC 2885 is attenuated by the prefilter at the highest velocities, but the Hα emission near the systemic velocity (which will be located near the minor axis of the galaxy) is not affected. The relationship between Hα and the nearby lines of [N II] at λ6548 and λ6583 is also shown in Figure 2. The [N II] lines are shown in their positions redshifted to the systemic velocity of UGC 2885 (Table 1) and also in their aliased positions. The relative line intensities of Hα and [N II] are drawn according to typical values for extragalactic H II regions (e.g., Garnett & Shields 1987; Searle 1971; Shields & Searle 1978): we take [N II] λ6548/Hα = 0.1 and [N II] λ6583/Hα = 0.3. Although the [N II] lines appear aliased close to Hα, their amplitudes are so attenuated by the prefilter that their contribution to our data is insignificant.

Lines at 6599 and 6610 Å from a calibration lamp were used to compute the effective gap. Individual quick-scanned data cubes (six cubes each night, two nights total) alternated with calibration observations. The frequent calibrations made possible individual correction for drifts of the optic axis and the effective etalon gap throughout the night. The data were "phase-calibrated" (Atherton et al. 1982) at full resolution (before Gaussian convolution) to convert the third axis of the data cube from "step" to wavelength by fitting a paraboloid of revolution to peaks in the emission profiles throughout each quick-stepped cube. The calibration data provided the velocity registration for cubes from the two nights of observation, and the spatial registration was done by fitting star positions and shifting before co-adding. Corrections were made to convert the velocities to a heliocentric system. The calibration of the data cubes, as well as the registration, co-adding, and spatial smoothing, was carried out using the GIPSY software system (Allen, Ekers, & Terlouw 1985) at the Kapteyn Institute, University of Groningen.

The typical seeing disk was 2″.7 FWHM. To increase the signal-to-noise ratio, data frames were spatially convolved with a Gaussian. The spatial resolution in the maps presented here, measured from stellar profiles on frames including continuum, is 4″.9 FWHM. The separation between channels is 11.24 km s^{-1}. For a typical finesse of $N \approx 25$, the free spectral range (FSR) of 81 channels implies a velocity resolution of about FSR/N = 3.2 channels (FWHM). The data were smoothed in velocity space with a 12321 ("pointed-hat") kernel, the effect of which is to decrease the velocity resolution to approximately $(3.2^2 + 3^2)^{1/2} = 4.4$ channels (FWHM), or $\sigma_v \approx 21$ km s^{-1}. We have independently estimated the final velocity resolution from a histogram of widths of Gaussians fitted to line profiles over the entire galaxy. Although the effective beam will usually contain many H II complexes and rotation could increase the measured line widths, some H II regions will be isolated within the beam. The low-width cutoff of the distribution of line widths is σ_v = 18–20 km s^{-1} (FWHM = 42–47 km s^{-1}), in good agreement with the estimate based on the FSR, a typical finesse, and the convolution kernel.

The continuum level was found to vary from frame to frame through the data cube, partly as a result of attenuation of the continuum by the prefilter, and partly owing to contamination by sunlight. A continuum emission image was isolated by averaging frames that were free from line emission. Continuum

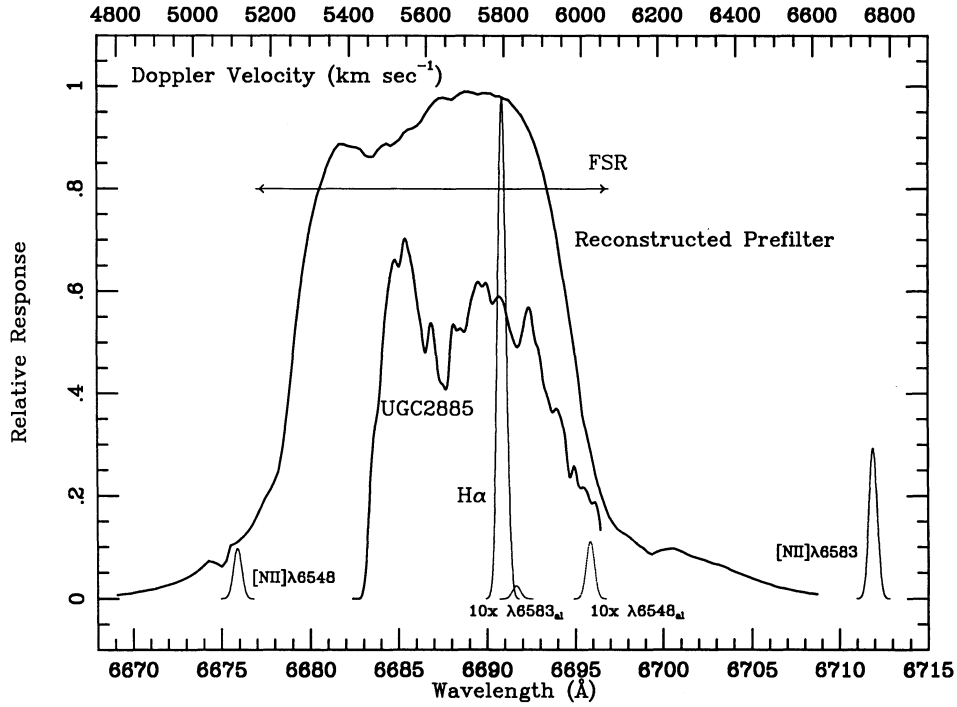

FIG. 2.—Schematic drawing of the wavelength responses, the data, and relevant line strengths. The prefilter shape was estimated from the spectrum of a bright star in the field (Fig. 1). The length of the double-headed arrow indicates the free spectral range (FSR). The Hα line is shown at its redshifted wavelength corresponding to the systemic velocity of UGC 2885. [N II] λ6548 and λ6583 are shown at their redshifted wavelengths with strengths relative to Hα typical of extragalactic H II regions. The [N II] lines are also shown at their aliased positions (subscript "al") attenuated by the prefilter. They are drawn at 10 times their real strengths and obviously do not contribute significantly to the measured emission. The total integrated spectrum of UGC 2885 is shown at arbitrary scale. Its cutoff at large wavelengths shows that Hα emission at high velocities is attenuated by the prefilter.

was subtracted to zero the mean level of bright stars in the field, yielding frames containing only Hα emission. Subtraction of the mean continuum leaves the profile baselines still perturbed by the solar spectrum from sunlight reflected from the Moon. Each frame was therefore further flattened by subtracting a two-dimensional cubic spline fitted to emission-free regions within the frame. Because UGC 2885 occupies less than half of the TAURUS field of view while reflected sunlight fills the frame, the final step of flattening each frame with a cubic spline will remove all remaining wide-field effects.

The data were corrected for the prefilter response by dividing each channel map by the value of the normalized prefilter function (Fig. 2) at the appropriate wavelength. Note in particular that the data near the minor axis were taken at the peak of the prefilter function, where the correction for prefilter response is negligible.

Figure 3 shows individual channels of the final, co-added, continuum-free (but not prefilter response–corrected) data cube. All subsequent figures will use data corrected for prefilter response. Prominent patches of emission are due to ionized gas in the disk of UGC 2885. The lowest contour is at 2 σ = 0.8 counts. The channel maps near the systemic velocity (5794 km s^{-1}, or near frame 10) illustrate the main observational result of this investigation: there are substantial velocity gradients in the motions of gas along the minor axis of UGC 2885. Isolated patches of emission in the individual channel maps near the systemic velocity appear on both sides of the minor axis. We know of no instrumental effects that could conspire to cause this behavior on a 10″ scale.

The integrated Hα intensity map is shown in Figure 4. A long spiral arm that curves to the northeast shows clearly. A spectrum of the bright H II complex at its end is shown in Figure 7. The outer spiral arm that curves to the southwest is fairly well defined; a spectrum of the brightest of three H II complexes at its end is shown in Figure 8. The centroid of the Hα peak in Figure 8 is close to the edge of the effective wavelength range (cf. Fig. 2). The spectra in Figures 7 and 8 are typical of H II concentrations in the galaxy and permit accurate determination of the velocity field of the ionized gas.

3. ANALYSIS

The velocity field of the ionized gas channel maps shown in Figure 3 was computed as the intensity-weighted mean velocity of the (prefilter response–corrected) emission profile at each position. Although it is formally correct, dividing by the prefilter function actually had little effect on the intensity-weighted mean velocities. The "response-corrected" velocities differed from "uncorrected" ones by about 3 km s^{-1} rms. Velocities near the minor axis were affected insignificantly by the correction. The computation was done using a suite of IRAF scripts (Gilmore & Allen 1990) that use a spatially smoothed intensity map as a mask for summing emission that appears in several contiguous channel maps above a threshold. The AIPS task BLANK was used to select regions of emission in each frame of the data cube. The IRAF scripts worked on the BLANKed cube. Regions of emission were selected by their persistence over three or more frames. (Noise in different frames is uncorrelated.) A movie made from the frames helped us to identify emission patches. We were able to recover more faint emission by applying the IRAF scripts to the BLANKed cube than by applying them to the full cube. The details of the velocity field in bright regions were the same, though, for computations on

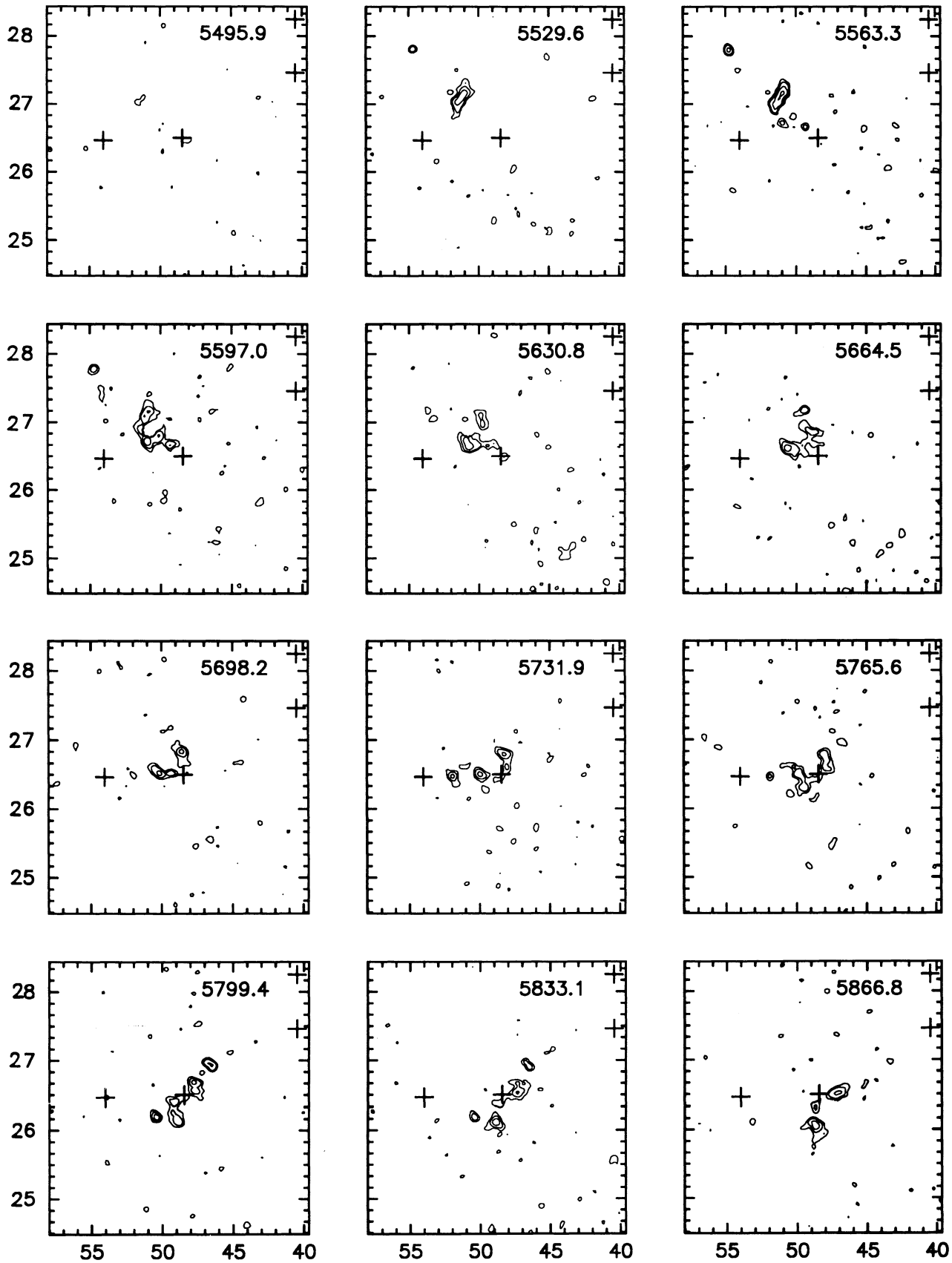

FIG. 3.—Individual channel maps of UGC 2885 are graphed with the lowest contour of 2 σ (where 1 σ is 0.4 counts) and logarithmic spacing, with successive levels separated by a factor of 2. Every third frame of the data cube is graphed here. The crosses mark the positions of the center of the galaxy and of bright stars in the field (Roelfsema & Allen 1985). Positions are $\alpha = 03^h49^m$ plus the horizontal axis label in seconds of time, and $\delta = +35°$ plus the vertical axis label in arcminutes (1950 epoch). Heliocentric recession velocities of the frames are listed in the upper right-hand corner in km s^{-1}. The systemic velocity of UGC 2885 is 5794 km s^{-1} (heliocentric), and $1' = 16.5\,h^{-1}$ kpc.

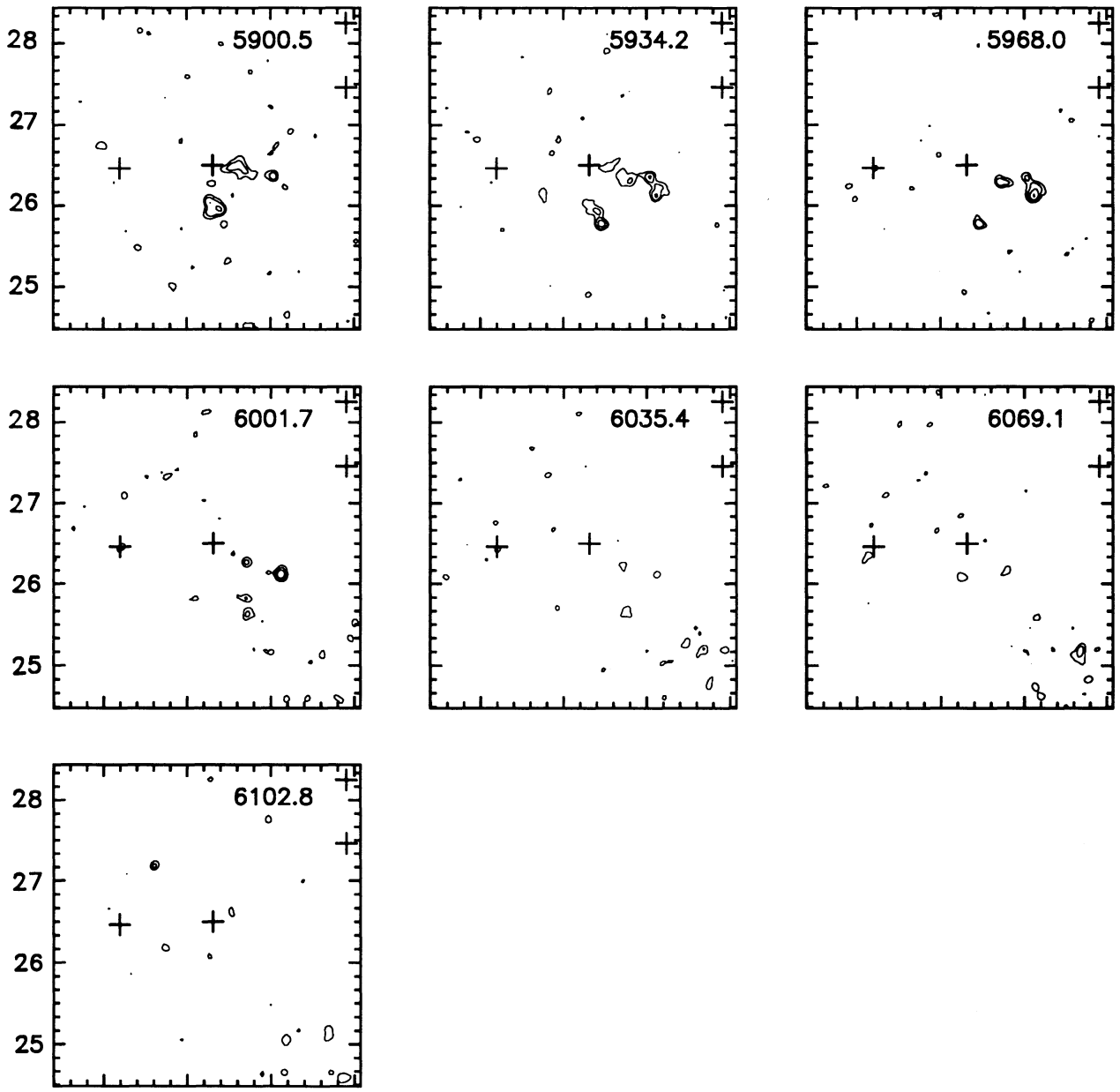

FIG. 3—*Continued*

the BLANKed and full data cubes. Figure 5 shows the velocity field in the plane of the sky; the separation between contours is 45 km s^{-1}. Bright stars in the northeast and southwest perturb the velocity determination and have been removed; their positions are marked by black dots in Figure 5. The radial motions[3] in the plane of the disk, identified in Figure 3 by the emission patches on both sides of the minor axis, are evident as wiggles in the isovelocity contours about the minor axis. These wiggles are particularly evident in the enlargement of the velocity field near the center of the galaxy (Fig. 6). Contours within the ellipse have been omitted because there the velocities are unreliable (see below, this section).

There was some concern that the observed radial motions along the minor axis could be the misleading product of anomalies in the data (such as noisy profiles or unforeseen consequences of the instrumental setup or calibration procedure) or shortcomings of the automated velocity field calculation. To secure confidence in the data, the velocity field was calculated independently by fitting a Gaussian plus a baseline to each emission profile using nonlinear least-squares optimization. All fitted profiles with great enough signal-to-noise ratio (where the noise level was calculated from an emission-free area on the baseline) were individually examined. Those fits that were poor were improved, if possible, by providing better initial parameters to the fitting algorithm. Only 4% of the pixels in Figure 4

[3] We caution the reader that the term "radial velocity" has two meanings. One meaning refers to radial motions along the line of sight, or observed radial velocities. The other refers to radial motions in the plane of the disk of a galaxy, or radial flows associated with spiral density waves. At each occurrence of the term "radial velocity" in this paper, we will make explicit the meaning we intend.

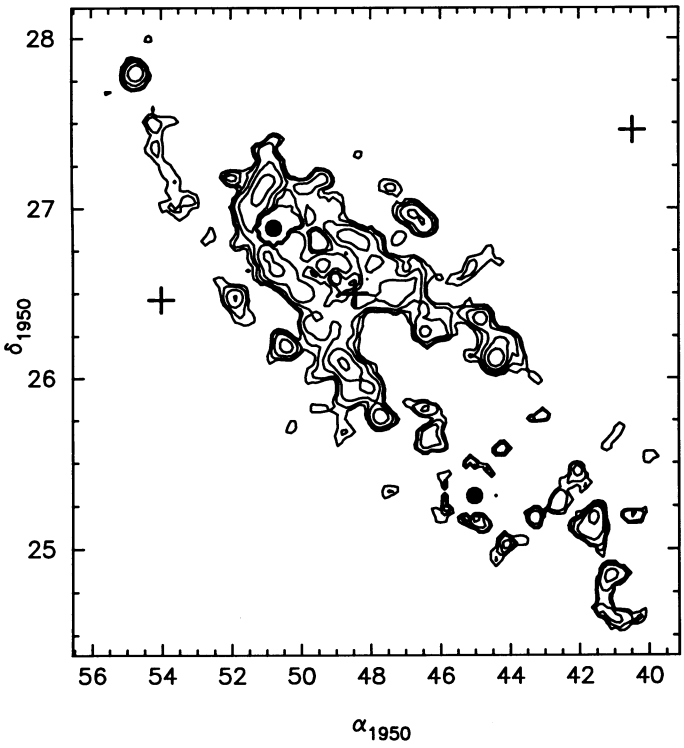

FIG. 4.—Integrated Hα (prefilter response–corrected) intensity map of UGC 2885. The lowest contour corresponds to the intensity of the sum of two 3 σ peaks in adjacent channels [that is (3 σ + 3 σ) × 11.24 km s^{-1} = 27 counts km s^{-1}]. Contours are logarithmically spaced, with successive levels separated by a factor of 2. The crosses mark the position of the center of the galaxy and of bright stars in the field (Table 1 and Roelfsema & Allen 1985). Bright stars in the northeast and the southwest that have been masked out of the figure are marked by solid dots. Spectra of the H II complexes at $03^h49^m55^s$ +35°27′50″ and $03^h49^m42^s$ +36°25′15″ are shown in Figs. 7 and 8.

have emission profiles with non-Gaussian shapes (extreme widths, especially near the center of the galaxy, or noisy peaks). The velocity field consisting of centroids of the fitted Gaussians compared very well with that generated from the IRAF scripts. The differences between velocities calculated by the two methods are characterized by a distribution with mean $\mu = 0.3$ km s^{-1} and width $\sigma = 3.4$ km s^{-1}. These statistics are for 3427 pixels.

Orientation parameters for UGC 2885 were computed using nonlinear least-squares optimization following the method of Warner, Wright, & Baldwin (1973). The location of the kinematic center, the systemic velocity, the position angle of the major axis, and the inclination were found that minimize the weighted sum of deviations from the mean velocity within concentric elliptical annuli. All annuli had the same center, position angle, and aspect ratio; these parameters were not allowed to vary with the radius of the annulus. This method will strongly weight high signal-to-noise ratio data, such as occur in the middle part of the disk. The total error is dominated by the less well-determined velocities in the outer disk, where the signal is falling, and by the relatively few positions near the center of the galaxy, which are affected by strong noncircular motions. The results are listed in Table 1. The systemic velocity coincides with the H I determination by Roelfsema & Allen (1985). The position angle of the line of nodes is within 1° of that measured by Roelfsema & Allen, although it is 5° from the value adopted by Rubin et al. (1980). The inclination is within 2° of the value determined by Roelfsema & Allen. The kinematic center is within 30″ of the H I determination by Roelfsema & Allen (their observations had a FWHM resolution of 14 × 23 arcsec^2). It is within 5″ of the optical center of the galaxy measured from a Palomar Sky Survey print (Roelfsema & Allen 1985). We estimate the 1 σ error of our kinematic center position to be ±4″. Our determination of the kinematic center position is graphed as a cross in Figures 5 and 6. The main observational results of this paper are not affected by a difference in the choice of the kinematic center position as large as 5″ from the adopted value.

Emission profiles near the center of the galaxy are very wide. Attenuation by the prefilter reduces the strength of very high velocity emission in our data. Therefore, the intensity-weighted mean velocities that are displayed in the velocity field maps (Figs. 5 and 6) are biased toward artificially low values at positions near the center of the galaxy, due both to a reduction in the amount of detectable high velocity emission and also to beam smoothing. An ellipse in Figure 6 contains the area in which the velocities are unreliable. We have drawn the boundaries of the ellipse where emission profiles along the major and minor axes have broadened and impinge on the prefilter half-power point.

Figure 9 shows the position-velocity diagram for a 4″.5 wide slice, or synthetic slit spectrum, along the major axis of the

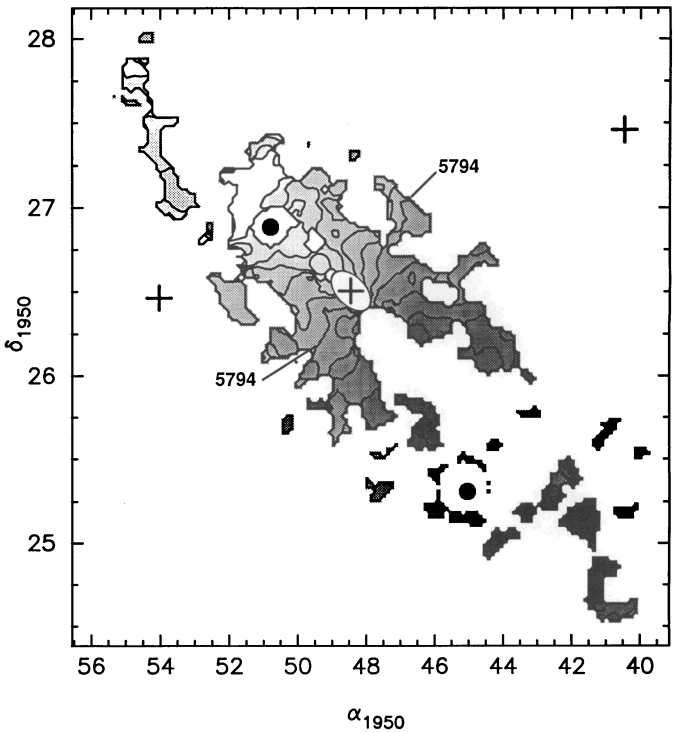

FIG. 5.—Hα (prefilter response–corrected) velocity field of UGC 2885 (radial velocities along the line of sight) computed as the intensity-weighted mean velocity. Coordinates are seconds of time from 03^h49^m on the horizontal axis and arcminutes from +35° on the vertical axis. The crosses mark the positions of the center of the galaxy and of bright stars in the field (Table 1 and Roelfsema & Allen 1985). The contours are spaced by 45 km s^{-1}; the contour corresponding to the (heliocentric) systemic velocity 5794 km s^{-1} is labeled. Darker shading corresponds to greater recession speed along the line of sight. Wiggles in the isovelocity contours near the minor axis exemplify radial motions in the disk across spiral arms (also see Fig. 6). Solid dots in the northeast and southwest mark the positions of bright stars, which perturb the velocity field and have been masked out of the data. Unreliable velocities near the center of the galaxy have been omitted.

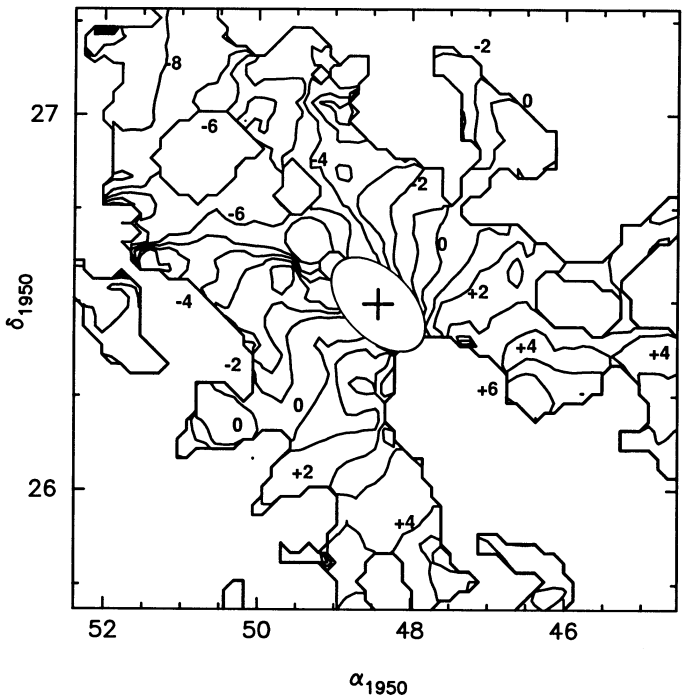

FIG. 6.—Expanded view of the velocity field (radial velocities along the line of sight) of the ionized gas near the center of the galaxy. Alternate contours are marked in units of 30 km s^{-1} from the (heliocentric) systemic velocity 5794 km s^{-1}, labeled "0." Contours marked "0" undulate back and forth across a line (the minor axis) passing through the cross. Velocities within the ellipse are unreliable because of the effects of beam smoothing and the attenuation of high velocity emission by the prefilter on the broad profiles there.

galaxy. Velocities in Figure 9 are along the line of sight. The vertical lines bound the region within which intensity-weighted mean velocities are unreliable (see above). The spatial and velocity resolution (FWHM) of the data is represented by the shaded circle at lower right. Also graphed (as crosses) for comparison are optical rotation curve data from Rubin et al. (1980; transcribed from Roelfsema & Allen 1985); some extreme velocity values from Rubin et al. have not been graphed because they are not relevant to our analysis.[4] The quickly rising rotation curve measured by Rubin et al. corresponds to the highest velocity emission near the center of the galaxy. The data from Rubin et al. generally follow the envelope of the major axis emission. The tendency of our data to fall below the Rubin et al. rotation curve is likely due to the 4".9 resolution of our data. Emission on either side of the major axis, which has a lower projected radial velocity along the line of sight, substantially contaminates our beam and biases each major axis profile (e.g., Figs. 7 and 8) toward a lower velocity.

There is strong emission near the center of the galaxy at very low velocities (Fig. 9). This emission lies within the vertical lines, which bound the region within which the intensity-weighted mean velocities are unreliable owing to the large widths of the profiles and the lower signal-to-noise ratio of the high-velocity emission. We are unable to decide with our data if the low velocities near the center are the result of fast rotation speeds or radial expansion in the central 500 pc. The broad velocity profiles in the central region of UGC 2885 should be studied further, but this subject lies outside the boundaries of the present paper.

[4] There is some confusion in the literature about the correct optical rotation curve of UGC 2885. Burstein et al. (1982) call attention to and claim to correct a computation error (involving only UGC 2885) in Rubin et al., but their corrected rotation curve values do not obviously reflect the correction they claim to apply.

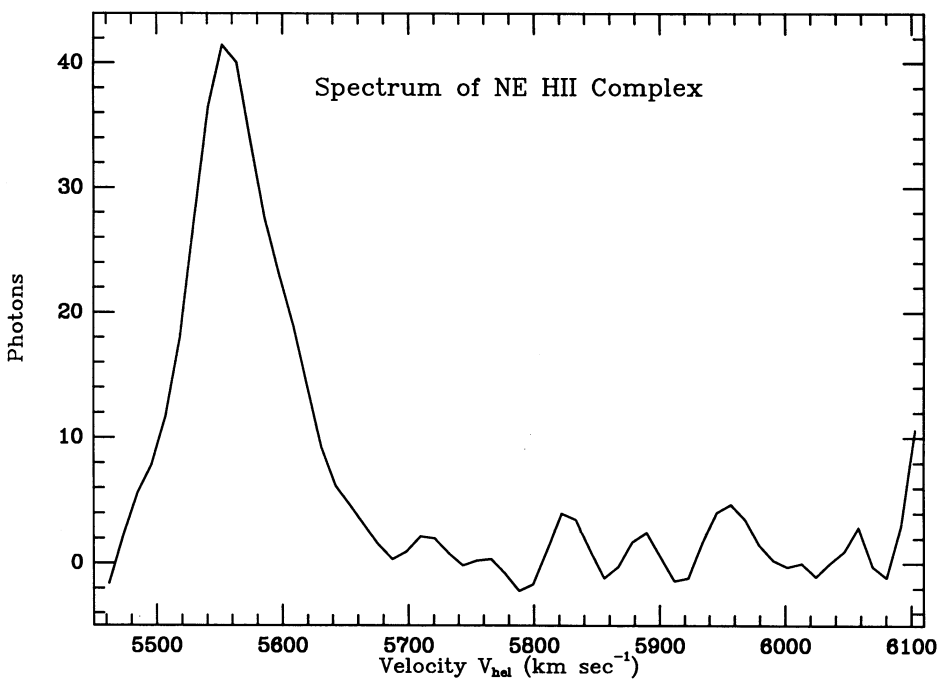

FIG. 7.—Spectrum (prefilter response–corrected) of the bright H II complex near the end of the outer spiral arm to the northeast. This figure is constructed from the sum of a 3 × 3 pixel region centered on the H II region.

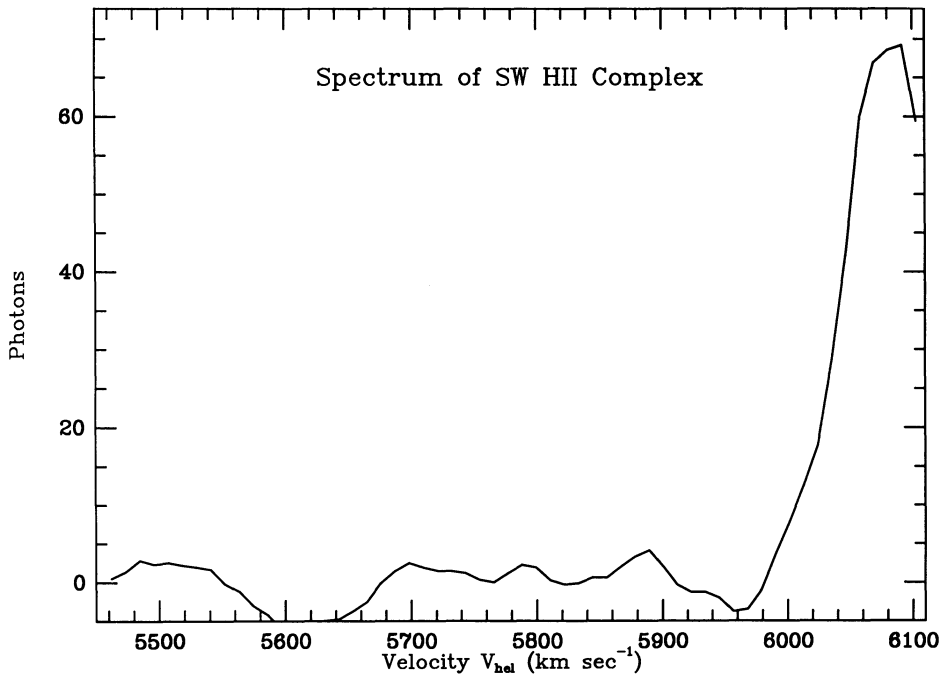

FIG. 8.—Spectrum (prefilter response–corrected) of the bright H II complex near the end of the outer spiral arm to the southwest. Emission is near the edge of the effective velocity range of the observations. This figure is constructed from the sum of a 3 × 3 pixel region centered on the H II region.

Figure 4 shows that Hα emission from the southwest part of the disk is missing from our data, and Figure 2 suggests that the reason for its disappearance is attenuation by the prefilter. Furthermore, the outline of the Hα "hole" is V-shaped in Figures 4 and 5, as expected for a galaxy with a rotation curve like that of UGC 2885 (Fig. 9) that rises steeply and then quickly flattens. It is therefore puzzling that the H II complex on the outer arm near the major axis to the southwest is visible at all. On a broad-band optical photograph (Rubin et al. 1980), the two outer arms are comparably bright, so it is unlikely that the southwest H II complex is enormously brighter and detectable despite the prefilter. Figure 9 shows that emission from the H II complexes in the southwest outer arm roughly coincide with a dip in the rotation curve defined by the slit spectrum data from Rubin et al. Because the recession speeds are 20–30 km s^{-1} lower there, the spectrum moves into our passband and produces a recognizable peak within our effective velocity range. We therefore confirm the structure in the major axis velocities of the outer disk measured by Rubin et al. Small discrepancies between our data and the rotation curve from Rubin et al. (noticeable near 2′ radius in Fig. 9) are due to the choice by Rubin et al. to adopt 50° as the position angle of the line of nodes. This value differs by 5° from that deduced from the full two-dimensional velocity field (Table 1). Slit spectrum data taken at position angles 40° and 43° were deprojected by Rubin et al. to the 50° line, thereby inflating the rotation speed and overestimating the corresponding radius compared with our major axis data (Fig. 9). We cannot undo their projection because data from both of their spectra are presented together and are not distinguishable.

The position-velocity diagram for a 4″.5 wide synthetic slit spectrum along the minor axis is shown in Figure 10. Velocities

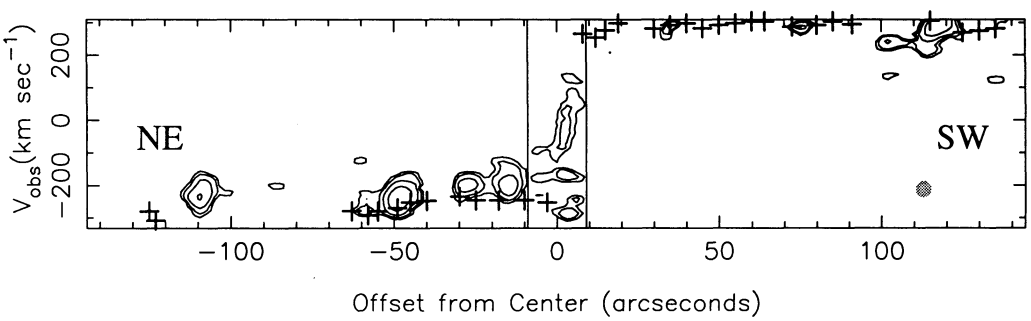

FIG. 9.—This is a position-velocity diagram for a 4″.5 wide slice along the major axis of UGC 2885, illustrating velocities along the line of sight. "NE" and "SW" refer to the northeast and southwest sides of the galaxy, respectively. The lowest contour is 2 σ, where σ is the noise in this figure computed from that in a single-channel map. (1 $\sigma = 0.4(3)^{1/2}$, since the slice is a sum 3 pixels wide.) The contours are logarithmically spaced with successive contours separated by a factor of 2. Spatial and velocity resolution (FWHM) is indicated by a shaded circle. The data (*crosses*) overlaid on the contour diagram are from the rotation curve measured by Rubin et al. (1980) from a long-slit spectrum. Emission is not evident on the southwest side where the velocities are higher and out of the effective velocity range of our observations. About 2″ from the center of the galaxy on the southwest side, the velocity falls enough to bring the emission into detectable range. Rubin et al. (1980) transformed their data onto a line of nodes different from the one we adopt (see § 3), causing small discrepancies with our data. The vertical lines correspond to the ellipse in Fig. 6 within which mean velocities are unreliably determined.

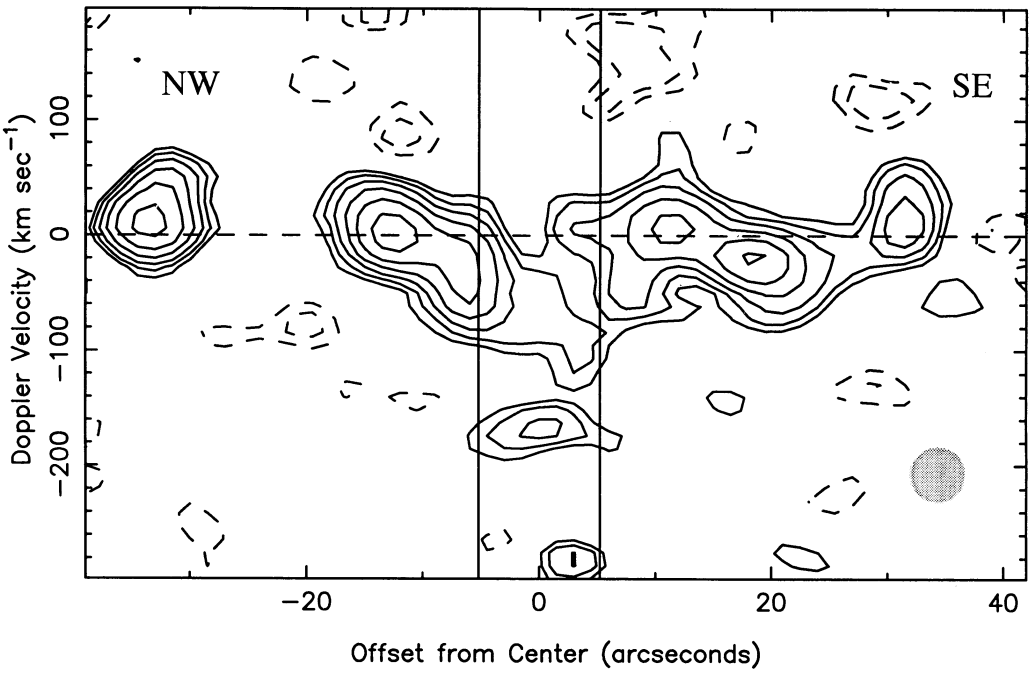

FIG. 10.—This is a position-velocity diagram for a synthetic slit along the minor axis. Velocities are along the line of sight with respect to the systemic velocity (5794 km s^{-1} heliocentric), which is drawn as a horizontal, dashed line. The lowest contour is 2 σ, where σ is the noise in this figure computed from that in a single channel map. ($1\ \sigma = 0.4(3)^{1/2}$, since the slice is a sum 3 pixels wide.) The contours are logarithmically spaced, with successive contours separated by a factor of 2. "NW" and "SE" refer to the northwest and southeast sides of the galaxy, respectively. Spatial and velocity resolution is indicated by the shaded circle.

in Figure 10 are along the line of sight. Emission is generally concentrated in spiral arms over well-defined velocity ranges and does not appear at all radii. Negative areas are represented by dashed contours; the prevalence of negative areas at high velocity is an artifact of inexact continuum subtraction owing to the steep edge of the prefilter. The shaded circle represents the spatial and velocity resolution (FWHM). Vertical lines bound the region within which intensity-weighted mean velocity computations yield unreliable results because of beam smoothing and the lack of detectable high velocity emission.

In Figure 11 are graphed the velocities in the plane of the disk at all pixels within a sector of 10° full opening angle centered on the minor axis with its apex at the center of the galaxy (Table 1). All the points in Figure 11 are not statistically independent; the pixels oversample the resolution by a factor of 3. The sizes of the graphical markers in Figure 11 correspond to the Hα line intensity for that point and indicate the relative reliability of the velocity data. Velocities between the vertical lines are unreliable because of beam smoothing and the attenuation of high velocity emission. The velocities entering Figure 11 were adjusted for projection effects by dividing by sin i, where i is the inclination; no correction was made for contamination by azimuthal motion due to rotation. The size of this correction is at most (298 km s^{-1}) sin (5° cos i) ≈ 12 km s^{-1} and is largest for points with the largest angles from the minor axis (at the edges of the sector). Ignoring this correction, which is uncertain at any particular point because the rotation curve in the absence of density wave streaming motions is not precisely known, adds to the scatter about the mean locus in Figure 11. Neglecting this correction, however, does not change the principal features of Figure 11. The figure, and frames near the 5799.4 km s^{-1} frame of Figure 3, constitute the central observational result of this paper.

The locations of spiral arm crossings on the minor axis are indicated by ranges between vertical arrows at the bottom of Figure 11. Spiral arm positions were measured from a print of a KPNO 4 m prime focus plate kindly provided by Vera Rubin. The arm widths are conservatively large owing to the limited resolution and detail of the print. We postpone our detailed interpretation of Figure 11 in terms of spiral density wave theories until a later paper. Some deductions (based on spiral density wave theory) are immediately suggested by Figure 11. Because the sign of the radial velocity changes with increasing radius on each side of the galaxy, we have observed gas both inside and outside its corotation radius. Furthermore, multiple sign changes on the same side imply that more than one pattern is present. A brief, introductory discussion of the relevance of our main results to spiral structure theory is presented in § 4.

We will now consider the reliability of the data. There is evidence that eliminates systematic errors as a possible source of the velocity gradients on the minor axis of UGC 2885 and that affirms our velocity scale. Possibilities that the radial velocity variations in the plane of the disk are caused by effects other than spiral density waves will also be considered.

We believe that no instrumental effects can cause the large velocity gradients measured along the minor axis. The velocity gradients are attributable to spatial differences in the local velocity field on a scale of 10″. They cannot be influenced by the prefilter or an incorrect determination of the etalon gap, both of which will contribute only to global variations across the field. The agreement between the rotation curve published by Rubin et al. (1980) and our position-velocity diagram for the major axis (Fig. 9) indicates that our velocity scale is correct (so the gap determination must also be correct). The absence of a large-scale velocity trend along the minor axis indicates that

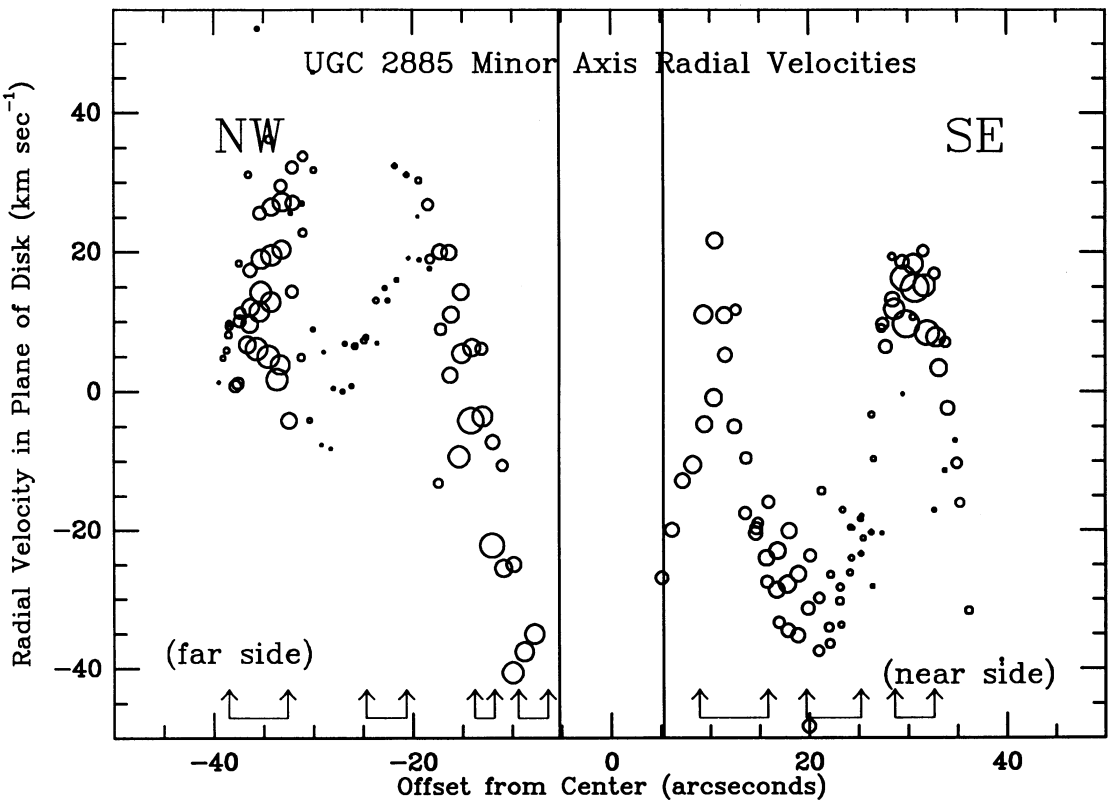

FIG. 11.—Radial velocities in the plane of the disk in a sector 10° wide along the minor axis are shown. These are noncircular motions mainly perpendicular to the spiral arms and have been corrected for the inclination of the galaxy to be velocities in the plane of the disk. "NW" and "SE" refer to the northwest and southeast sides of the galaxy, respectively. "Near" and "far" side labels assume trailing spiral arms. Negative velocities are approaching, positive are receding. The magnitudes of the velocity variations are large and may be the result of a strong spiral density wave that persists even in the outer disk. The size of the graphical markers corresponds to the integrated line intensity for that velocity measurement and illustrates the relative reliability of that measurement. Larger circles represent greater integrated intensities; a range of a factor of 15 in intensity is displayed. Mean velocities between the vertical lines are unreliably determined. Positions of spiral arm crossings are indicated as ranges between vertical arrows at the bottom of the graph.

the velocities we compute are spatially stable (so any varying continuum introduced by the prefilter and not adequately subtracted in our data processing is inconsequential).

Peculiar geometry or anomalous line profiles cannot cause the observed velocity gradients. A velocity is assigned to each spatial position based on the intensity-weighted mean velocity there; these weighted means compare well with the centroid velocities of fitted Gaussian profiles (§ 3). Because only radial motion in the disk is observed along the minor axis, a superposition of arms can only broaden profiles and thus diminish the existing velocity gradients; it cannot amplify them. It is possible that motions in the z-direction in a warped disk could lead to velocity gradients of the type observed, but no sign of a large-scale warp has been seen in H I data (Roelfsema & Allen 1985). Ambiguities in velocity owing to irregular profiles that could have caused spurious velocity gradients were avoided with the profile fitting procedure. Furthermore, peculiar emission profiles were rare (comprising only 4% of the pixel positions on the sky with measured Hα emission), and they did not unduly influence minor axis velocity determinations. The velocity fields resulting from profile fitting and from intensity-weighted averaging were in excellent agreement.

Our measurements do have a simple, geometric shortcoming: we do not measure velocities precisely perpendicular to the spiral arms. Instead, since the arms have a significant pitch angle (roughly 30° in the outer disk: Roelfsema & Allen 1985), the projection of the gas velocity along the line of sight contains components perpendicular to the arm and (in small part) parallel to the arm. This contamination complicates the comparison of our data with calculations based on spiral density wave theory. Fortunately, the high inclination of UGC 2885 reduces this effect, which is at most about (50 km s^{-1}) sin (α cos i) = 12 km s^{-1}, since peak radial and azimuthal perturbed flow velocities are about the same. Here, α is the pitch angle (about 30°: Roelfsema & Allen), and i is the inclination.

4. DISCUSSION

4.1. *Radial Flows and Spiral Density Waves*

The magnitude of the radial motions across spiral arms in UGC 2885 is 50–70 km s^{-1} peak-to-peak in the plane of the galaxy on each side of the center (Fig. 11). Radial velocities of this order have been measured in the disks of other spiral galaxies as well. The peak-to-peak radial motions across arms in the plane of M81 are of order 30 km s^{-1} from H I measurements (Visser 1980b); those in M51 are of order 60–90 km s^{-1} from CO measurements (Vogel et al. 1988) and from Hα Fabry-Perot observations (Tilanus & Allen 1991).

The corroboration of the measurements listed above suggests that spiral density waves are similar in all the galaxies with a strong spiral pattern that have been studied. However, there are some notable exceptions. It is puzzling that radial motions in the plane of the disk comparable to those measured with CO and Hα data have not been detected in M51 with H I

measurements. To compound the puzzle, there is no confirmation of any radial motion across spiral arms in M83 from Fabry-Perot observations (Tilanus 1990; Tilanus & Allen 1992).

The magnitude of the velocity streaming across spiral arms in those galaxies in which variations are detected is so large that the spiral potential is probably quite deep. (In M51, the uncertainty in the inclination of the galaxy may appreciably inflate the computed velocities in the plane of the disk.) Shu et al. (1973) computed the nonlinear response of gas to steady forcing by spiral potentials in a model galaxy similar to our own. The peak-to-peak variations in gas velocity across spiral arms they computed ranged from 27 km s^{-1} near the solar circle (agreeing with a similar model by Roberts 1969, who computed a value of about 30 km s^{-1}) to a mere 11 km s^{-1} well outside the solar circle, both for a forcing potential 5% of the axisymmetric potential. (The latter value boosts to 19 km s^{-1} for a 7% forcing potential.) These velocities are comparable with those observed in M81. Streaming velocities scale linearly with the rotation speed of the galaxy, so to compare the models of our Galaxy with UGC 2885, for example, multiply by the ratio of the asymptotic speeds, or $300/250 \approx 1.2$. The size of the total velocity variation perpendicular to spiral arms grows roughly linearly with the strength of the forcing potential (see Visser 1978, his Fig. 5.3), so it is conceivable that the relatively large velocities across the spiral arms of UGC 2885 and M51 could result from correspondingly stronger spiral potentials, say 10%–15%. Such strong potentials will be accompanied by increased gas compression in shocks. The resolution in H I (Roelfsema & Allen 1985) is insufficient to estimate the gas compression in UGC 2885. It is not clear at what level of forcing the spiral density wave models break down because of highly nonlinear gas response, nor whether the large observed velocities across arms imply that UGC 2885 is in the highly nonlinear regime.

Because the pitch angle, at least for the outer spiral arms, is rather large, about 30° (Roelfsema & Allen 1985), large variations in the radial velocities across arms are expected. There is a substantial component of the orbital circular velocity perpendicular to an open spiral arm. As a consequence of the shock, the gas upstream from the arm loses most of this speed and becomes subsonic. (We are thinking here of gas inside the corotation radius of the pattern.) The spiral arm potential will continue to grow until such a strong shock is possible, then the nonlinearity will probably suppress further growth. Thus, strong shocks and large radial flow speeds in the disk should accompany open spiral arms, and this will be further enhanced for larger galaxies.[5]

A more conjectural argument suggests that large spiral galaxies may naturally have stronger spiral density waves, particularly in the outer parts of their disks. The velocity dispersion of the stars in the disk of spiral galaxy increases with the galaxy's age principally because of encounters of stars with giant molecular clouds (Spitzer & Schwarzschild 1953). The rate of increase of the stellar velocity dispersion depends on the local differential rotation (for long impact parameters, although small impact parameters may have a larger total effect: cf. Binney & Tremaine 1987). In large galaxies, the differential rotation in the outer disk is small, so the velocity dispersion will increase more slowly there than in the inner disk. If the velocity dispersion is lower, then Toomre's Q (a measure of the stability of the disk: Toomre 1964) will be lower in the outer disks of larger spiral galaxies. Therefore, spiral structure will be more amplified in larger disk galaxies owing to their lower Q values (cf. Toomre 1981). The disk of UGC 2885, in particular, is dynamically younger than that of many spiral galaxies: the outer disk of UGC 2885 has made only a dozen revolutions in a Hubble time.[6]

Despite the similarity of the magnitudes of velocities across spiral arms in M51 and UGC 2885, there are differences between these two galaxies that are significant. These difference must be addressed if analogies are drawn between the spiral structure in M51 and UGC 2885. With an estimated Holmberg diameter of 168 h^{-1} kpc, UGC 2885 is 4 times larger than M51, whose Holmberg diameter is only 40 kpc (Holmberg 1958; Sandage & Tammann 1975), and UGC 2885 is 6–21 times more massive than M51. (Depending on the interpretation of the M51 rotation curve and if its disk is warped, the asymptotic rotation speed at 17 kpc radius is 115–220 km s^{-1} [Tully 1974].) The companion of M51 (NGC 5195) has almost certainly influenced the spiral structure of M51 (cf. Toomre 1972; Howard & Byrd 1990). More controversial is the possibility that the spiral density waves in M51 are substantially stronger as a result of forcing by the companion. It is not clear if UGC 2885 has any companions, although there are two candidates in the field nearby. We will address the possibility that these nearby galaxies are physical companions in a subsequent paper. It is clear, though, that UGC 2885 has no NGC 5195–like companion: the field galaxies are small, relatively distant, and show no obvious signs of interaction with UGC 2885, quite in contrast with NGC 5195. By driving the spiral density waves in M51, NGC 5195 may cause greater wave amplitudes and accompanying flow speeds than would be possible for self-excited waves in the same disk. Since UGC 2885 lacks a companion with a comparable mass as nearby as NGC 5195 is to M51, ionized gas in the disk of UGC 2885 must derive its large radial flow velocities from intrinsic disk properties. As stated above, more open spiral patterns demand larger radial flow speeds. This fact alone distinguishes UGC 2885 from M51, whose spiral arm pitch angle is only about 12° (Considère & Athanassoula 1988). Furthermore, if the disk of UGC 2885 had a value of the stability parameter Q near unity, larger spiral density wave growth factors would result. Although there is still much to be learned before spiral structure is well understood, the theories indicate that there should be no difference between self-excited and driven spiral density waves in the same disk. If this is true, then the similar radial flow speeds in the disks of UGC 2885 and M51 can only be explained by a similarity in the physical parameters of their disks, namely, similar Q values or (in modal theory) growth rates. In a subsequent paper, we will present self-consistent models of the disk of UGC 2885 that we can use to compare UGC 2885 with theoretical predictions for spiral structure in such a disk.

5. CONCLUSIONS

The velocity field of the giant spiral galaxy UGC 2885 has been mapped in Hα emission at 5″ resolution using the TAURUS I imaging Fabry-Perot spectrometer. The velocity field shows strong perturbations; radial flows across spiral arms are particularly evident along the minor axis. The flows are obvious in several channel maps where emission is seen on

[5] We are grateful to S. Lubow for showing us this argument.

[6] We are grateful to J. Sellwood for suggesting this argument to us.

both sides of the minor axis. The amplitude of the peak-to-peak variation in the radial motions in the plane of the galaxy along the minor axis is 50–70 km s^{-1}. The strength of the spiral density wave, if self-excited, may result from any of at least three factors, or a combination of them: the openness of the spiral arms, the great size and/or mass of the galaxy, or a rather large spiral forcing potential of perhaps 10%–15%.

We thank the staff at La Palma Observatory for their excellent support during our observing program there. We especially appreciate the efforts of Paul Atherton and Keith Taylor, who conceived of the TAURUS instrument and conducted the observing program with it at La Palma. We also thank Diane Gilmore, who wrote software that eased analysis of the data cube. B. C. is especially grateful to Steve Lubow and Jerry Sellwood, who generously gave much time for discussion and sage advice. This research was supported in part by the Director's Research Fund at the Space Telescope Science Institute.

REFERENCES

Allen, R. J., Atherton, P. D., & Tilanus, R. P. J. 1986, Nature, 319, 296
Allen, R. J., Ekers, R. D., & Terlouw, J. P. 1985, in Data Analysis in Astronomy, ed. V. Di Gesù, L. Scarsi, P. Crane, J. H. Friedman, & S. Levialdi (New York: Plenum), 271
Atherton, P. D., Taylor, K., Pike, C. D., Harmer, C. F. W., Parker, N. M., & Hook, R. N. 1982, MNRAS, 201, 661
Binney, J. M., & Tremaine, S. 1987, Galactic Dynamics (Princeton: Princeton Univ. Press)
Boksenberg, A. 1972, in Auxiliary Instrumentation for Large Telescopes, Proc. ESO/CERN Conference, ed. S. Laustsen & A. Reiz (Geneva: ESO), 295
Burstein, D., Rubin, V. C., Thonnard, N., & Ford, W. K., Jr. 1982, ApJ, 253, 70
Considère, S., & Athanassoula, E. 1988, A&AS, 76, 365
Fabry, C., & Perot, A. 1902, ApJ, 15, 73
Garnett, D. R., & Shields, G. A. 1987, ApJ, 317, 82
Gilmore, D., & Allen, R. J. 1990, BAAS, 22, 1327
Giovanardi, C., & Hunt, L. K. 1988, AJ, 95, 408
Guhathakurta, P., van Gorkom, J. H., Kotanyi, C. G., & Balkowski, C. 1988, AJ, 96, 851
Holmberg, E. 1958, Medd. Lunds Astron. Obs., II, 136
Howard, S., & Byrd, G. G. 1990, AJ, 99, 6
Huchtmeier, W. K. 1975, A&A, 72, 73
Jacoby, G., Ciardullo, R., & Ford, H. C. 1990, ApJ, 356, 332
Nilson, P. 1973, Uppsala General Catalogue of Galaxies (Uppsala: Uppsala General Offset Center AB).
Pence, W. D., Taylor, K., & Atherton, P. 1990, ApJ, 357, 415
Roberts, M. S., & Whitehurst, R. N. 1975, ApJ, 201, 327
Roberts, W. W. 1969, ApJ, 158, 123
Roelfsema, P. R., & Allen, R. J. 1985, A&A, 146, 213
Rubin, V. C., Ford, W. K., Jr., & Thonnard, N. 1980, ApJ, 238 471
Sandage, A., & Tammann, G. A. 1975, ApJ, 196, 313
———. 1981, A Revised Shapley-Ames Catalog of Bright Galaxies (Washington, DC: Carnegie Institution of Washington)
Searle, L. 1971, ApJ, 168, 327
Shields, G. A., & Searle, L. 1978, ApJ, 222, 821
Shu, F. H., Millione, V., & Roberts, W. W., Jr. 1973, ApJ, 183, 819
Smoot, G. F., et al. 1991, ApJ, 371, L1
Spitzer, L., & Schwarzschild, M. 1953, ApJ, 118, 106
Tilanus, R. P. J. 1990, Ph.D. thesis, Univ. of Groningen
Tilanus, R. P. J., & Allen, R. J. 1989, ApJ, 339, L57
———. 1991, A&A, 244, 8
———. 1992, A&A, submitted
Toomre, A. 1964, ApJ, 139, 1217
———. 1981, in The Structure and Evolution of Normal Galaxies, ed. S. M. Fall & D. Lynden-Bell (Cambridge: Cambridge Univ. Press), 111
Toomre, A., & Toomre, J. 1972, ApJ, 178, 623
Tully, R. B. 1974, ApJS, 27, 437
Vaughan, J. M. 1989, The Fabry-Perot Interferometer (Bristol: Adam Hilger)
Visser, H. C. D. 1978, Ph.D. thesis, Univ. of Groningen
———. 1980a, A&A, 88, 149
———. 1980b, A&A, 88, 159
Vogel, S. N., Kulkarni, S. R., & Scoville, N. Z. 1988, Nature, 334, 402
Warner, P. J., Wright, M. C. H., & Baldwin, J. E. 1973, MNRAS, 163, 163